Predictive modelling of thermo-active tunnels in London Clay

Klementyna A. Gawecka [1]

Wenjie Cui [1] *

David M.G. Taborda [1]

David M. Potts [1]

Lidija Zdravković [1]

Alexandros Loukas [2]

[1] Department of Civil and Environmental Engineering, Imperial College London, London, UK

[2] Atkins, Epsom, UK (formerly Imperial College London)

* Corresponding author: w.cui11@imperial.ac.uk

Abstract

Thermo-active structures are underground facilities which enable the exchange of thermal energy between the ground and the overlying buildings, thus providing renewable means of space heating and cooling. Although this technology is becoming increasingly popular, the behaviour of geotechnical structures under additional thermal loading is still not fully understood. This paper focuses on the use of underground tunnels as thermo-active structures and explains their behaviour through a series of finite element analyses based on an existing case study of isothermal tunnels in London Clay. The bespoke finite element code ICFEP is adopted which is capable of simulating the fully coupled thermo-hydro-mechanical behaviour of porous materials. The complex coupled interactions between the tunnel and the surrounding soil are explored by comparing results from selected types of coupled and uncoupled simulations. It is demonstrated that: (1) the thermally-induced deformation of the tunnel and the ground are more critical design aspects than the thermally-induced forces in the tunnel lining, and (2) the modelling approach in terms of the type of analysis, as well as the assumed permeability of the tunnel lining, have a significant effect on the computed tunnel response and, hence, must be chosen carefully.

Keywords: ground movements; numerical modelling; tunnels & tunnelling; temperature effects; soil/structure interaction

Notation

A_1, m, n	parameters for calculating the elastic shear modulus
A_2	coefficient of the hardening modulus
a, b, r, s	degradation parameters
c'	cohesion
E	Young's modulus
E_d	deviatoric strain invariant
G_{max}	maximum shear modulus
G_{min}	minimum shear modulus
G_{ref}	maximum shear modulus at a reference mean effective stress
G_{tan}	tangent shear modulus
K	bulk modulus
K_f	bulk modulus of pore fluid
K_{max}	maximum bulk modulus
K_{min}	minimum bulk modulus
K_{ref}	maximum bulk modulus at a reference mean effective stress
K_{tan}	tangent bulk modulus
K_0	coefficient of earth pressure at rest
k_T	thermal conductivity
m_G, m_K	parameters defining the dependence of elastic stiffness on mean effective stress
p'	mean effective stress
p_f	pore fluid pressure
p'_{ref}	reference mean effective stress
q_f	pore fluid flow
q_T	heat flux
R	ratio of the yield surface size to that of the bounding surface
$R_{G,min}$	minimum normalised value of G_{tan}
$R_{K,min}$	minimum normalised value of K_{tan}
T	temperature
u_x	horizontal displacement
u_y	vertical displacement
α_f	linear thermal expansion coefficient of pore fluid

62	α_s	linear thermal expansion coefficient of soil skeleton
63	γ_s	unit weight of soil
64	ε_{vol}	volumetric strain invariant
65	κ	slope of swelling lines in $\nu - lnp'$ space
66	λ	slope of the normal compression line in $\nu - lnp'$ space
67	μ	Poisson's ratio
68	ν	specific volume
69	ν_1	specific volume at unit pressure in $\nu - lnp'$ space
70	ρC_p	volumetric heat capacity
71	φ'	angle of shearing resistance
72	ψ'	angle of dilation

1 Introduction

Due to the rising awareness of the negative impacts of burning fossil fuels on the environment, as well as diminishing resources, the interest in renewable energy sources has been growing. The resulting rapid technological advancement continuously improves the efficiency and reduces the cost of renewable energy systems. The utilisation of low enthalpy geothermal energy, which is the thermal energy beneath the earth's surface associated with temperatures up to 40 ˚C and usually depths up to 100 m (Banks, 2012), is a particularly attractive solution as it provides a clean and reliable means of space heating and cooling. The ground temperature below a depth of 10-15 m, being unaffected by the seasonal changes in solar radiation, is higher than winter air temperatures and lower than the summer air temperatures, thus allowing the ground to be used as a heat source in the winter and a heat sink in the summer. The transfer of this thermal energy between the ground and the building is possible, for example, by circulating a fluid through a series of pipes (the so-called heat exchanger pipes) buried in the ground. A major advantage of these closed-loop ground source energy systems (GSES) is that they can be incorporated into underground structures, such as piled foundations, retaining walls or tunnel linings, which are consequently termed thermo-active structures.

The focus of the research presented in this paper is on thermo-active tunnels which have been studied to a lesser extent than thermo-active piled foundations (e.g. Laloui *et al.*, 2006; Bourne-Webb *et al.*, 2009; Gawecka *et al.*, 2017) or retaining walls (e.g. Bourne-Webb *et al.*, 2016; Sterpi *et al.*, 2018; Sailer *et al.*, 2019). Tunnel linings are potentially very effective heat exchangers due to their large surface area in contact with the ground. The heat exchanger pipes can be installed by either embedding them in prefabricated tunnel lining segments, or by attaching them to a geotextile placed between the primary and secondary concrete lining (Bourne-Webb & Gonçalves, 2016). The energy extracted from the surrounding soil, as well as the air inside the tunnel can be utilised for heating of the overlying buildings, enabling cooling of the tunnels at the same time.

The use of tunnels as thermo-active structures is far less common than piled foundations or retaining walls, perhaps due to a greater relative risk of tunnelling projects exacerbated by a lack of understanding of how they behave under thermal loading. So far, the scheme has been incorporated into parts of the Vienna Metro, the Vienna main sewer, the Lainzer Tunnel (Brandl, 2006; Adam & Markiewicz, 2009) and the Jenbach Tunnel in Austria (Franzius & Pralle, 2011; Buhmann *et al.*, 2019), an abandoned railway tunnel in South Korea (Lee *et al.*, 2012), the Linchang Tunnel in China (Zhang *et al.*, 2014), and the Stuttgart Fasanenhof Tunnel in Germany (Buhmann *et al.*, 2016). The tunnels were equipped with temperature sensors which allowed their thermal performance and the changes in ground temperature due to their operation to be studied. The results of these full-scale field tests are discussed by Franzius & Pralle (2011), Lee *et al.* (2012), Zhang *et al.* (2014) and Buhmann *et al.* (2016). Furthermore, experiments on a 0.4 m in dimeter and 1.2 m in length model thermo-active tunnel placed in a sand box were performed by Zhang *et al.* (2016) and Zhang *et al.* (2017), who investigated its thermal performance in conditions with groundwater flow. More recently, Barla *et al.* (2019) presented an experimental study on a 2.8 m long real-scale prototype of a thermo-active tunnel lining instrumented with temperature, stress and strain sensors, thus allowing investigation of thermal, as well as structural performance. A preliminary heating mode test measured extracted thermal power of 51 W/m^2 and showed that the stresses and strains in the lining resulting from the thermal operation appear to be of the same order of magnitude as those experienced during normal seasonal temperature changes.

Although the field and laboratory tests provide an invaluable insight into the behaviour of thermo-active tunnels, numerical modelling enables extensive exploratory studies of a tunnels' response under a wide variety of scenarios. For example, finite element (FE) analyses were performed to investigate the feasibility of implementing the geothermal energy technology into tunnelling projects such as the Turin Metro Line 1 South Extension (Barla *et al.*, 2016) or Warsaw Metro NE extension (Baralis *et al.*, 2018). Additionally, a parametric study involving the Turin Metro Line 1 South Extension was carried out by Di Donna & Barla (2016) who varied the subsoil initial temperature, groundwater, flow velocity and ground thermal conductivity. Following the validation of their numerical model by reproducing the response of the Stuttgart Fasanenhof Tunnel, Bidarmaghz *et al.* (2017) and Bidarmaghz & Narsilio (2018) explored the effects of various groundwater flow directions and rates.

The above numerical studies involve thermo-hydraulic FE analyses, and therefore, investigate only the thermal performance of thermo-active tunnels. In order to explore the structural performance, the mechanical behaviour of the tunnel lining must be explicitly accounted for in the model. Nicholson *et al.* (2013) carried out thermo-mechanical FE analyses which predicted a 7% increase in the hoop stress due to an energy extraction rate of 30 W/m^2, whereas Barla & Di Donna (2018) adopted a thermo-mechanical finite difference model which showed maximum stress changes of 1 MPa within the tunnel lining due to a temperature change of 10 ˚C. However, the deformation of the tunnel or the response of the surrounding soil were not considered in either of the two studies.

While the currently published research on thermo-active tunnels is valuable, it does not fully explore all aspects of their behaviour, especially the effects of thermal loading on the mechanical response of the tunnel and the seepage and deformation behaviour of the surrounding soil. Therefore, the aim of this paper and its principle novelty is to quantify in detail the soil-structure interaction phenomena occurring in problems involving thermo-active tunnels, and to explain the transient fully coupled thermo-hydro-mechanical (THM) behaviour resulting from thermally activating these structures. This is achieved by performing a series of coupled THM analyses using the Imperial College Finite Element Program (ICFEP, Potts & Zdravković, 1999). The tunnelling project chosen for this study is the Crossrail underground line at Hyde Park in London, UK. Although the Crossrail tunnels are not thermo-active, they represent a typical modern tunnel with a bolted precast concrete segmental lining, constructed using an earth-pressure-balance tunnel-boring machine in ground conditions characteristic of the London Basin. Additionally, their construction was extensively monitored (Wan *et al.*, 2017) and their response was successfully reproduced through FE analysis employing coupled consolidation and advanced constitutive models (Avgerinos *et al.*, 2018). In this study, the analyses performed by Avgerinos *et al.* (2018) were reproduced using the same modelling methods and, subsequently, coupled THM analyses simulating the long-term thermal operation of the tunnels were carried out. The results of the latter stage are presented and discussed in this paper. As far as the authors are aware, this study is the first to explore the fully coupled THM behaviour of the thermo-active tunnel lining and the surrounding ground.

2 Numerical model

2.1 Site and ground characteristics

The ground profile proposed by Avgerinos *et al.* (2018) based on the borehole data obtained by Wan & Standing (2014) was adopted in this study. It consists of 6 m of superficial deposits (made ground, alluvium and terrace gravels) overlying London Clay divided into three units (King, 1981): B2, A3 and A2 with thicknesses of 30 m, 12.5 m and 11.4 m, respectively. The underlying Lambeth Group was divided into an upper layer with more clayey and less permeable soil of thickness of 4.7 m, and a 6 m thick more granular and more permeable lower layer. The two Crossrail tunnels were constructed in the B2 and A3 units of the London Clay with the centres of the tunnels at a depth of 34.2 m below ground level (bgl) and a centre-to-centre spacing of 15.2 m. The tunnels were lined with precast concrete segmental rings with an internal diameter of 6.2 m and external diameter of 6.8 m. The stratigraphy and the geometry of the problem are depicted in Figure 1.

2.2 Analysis stages

Table 1 presents the stages of the numerical analysis performed in this study. Stages 1 to 4 involve modelling of the previous stress history of the site, which is vital for accurate predictions of tunnelling effects (Avgerinos *et al.*, 2016), as well as the installation of the Crossrail tunnels. As these stages are the exact repetition of isothermal analyses carried out by Avgerinos *et al.* (2018), their results are not discussed in this paper. Stage 5 is a long-term isothermal coupled consolidation analysis during which all previously generated excess pore water pressures are allowed to dissipate in order to separate the thermal from the excavation effects (Gawecka *et al.*, 2017). The focus of this paper is Stage 6 which involves a series of coupled THM analyses simulating the hypothetical long-term thermal operation of the Crossrail tunnels.

Table 1 Stages of the numerical analysis

Stage 1	Uncoupled – Drained	Erosion of 180 m of overburden Deposition of the superficial deposits and a rise of the groundwater table from the top of the London Clay to a 3 m depth bgl
Stage 2	Coupled consolidation	Underdrainage of the pore water pressure profile
Stage 3	Coupled consolidation	Excavation of the westbound (WB) tunnel and construction of its tunnel lining Consolidation period of 73 days
Stage 4	Coupled consolidation	Excavation of the eastbound (EB) tunnel and construction of its tunnel lining
Stage 5	Coupled consolidation	Consolidation period allowing full dissipation of the excess pore water pressures generated in Stages 3 and 4
Stage 6	Coupled THM	Thermal operation of the tunnels

2.3 Analysis details

2.3.1 Finite element mesh

The finite element mesh for the coupled THM plane strain analyses preformed in this study is shown in Figure 1. The soil and the tunnel lining were discretised with eight-noded quadrilateral elements where each node has two displacement degrees of freedom. As London Clay and the Upper Lambeth Group were modelled as consolidating materials, pore water pressure degrees of freedom were assigned to the corner nodes of the elements representing these materials. During the non-isothermal stage of the analysis (i.e. Stage 6), all the elements representing the soil layers had additional temperature degrees of freedom at all nodes.

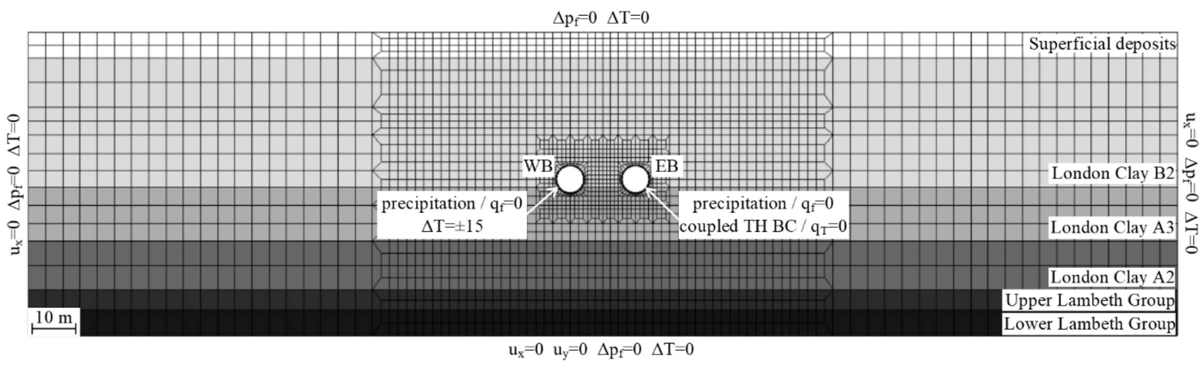

Figure 1 Finite element mesh with stratigraphy, indication of the westbound (WB) and eastbound (EB) tunnels and boundary conditions

2.3.2 Material models and properties

The first part of this study involved reproduction of the isothermal analyses performed by Avgerinos *et al.* (2018), with the same material properties being adopted as summarised in Tables 3-7 in the Appendix. The superficial deposits comprising of made ground, alluvium and terrace gravels were modelled as linear elastic-perfectly plastic with a Mohr Coulomb failure surface, whereas the Lambeth Group layers were modelled as non-linear elastic-perfectly plastic with a Mohr Coulomb failure surface. Although Avgerinos *et al.* (2018) adopted the Jardine *et al.* (1986) small strain stiffness model to represent the non-linear elastic behaviour, in this study, the Imperial College Generalised Small-Strain Stiffness (IC.G3S, Taborda *et al.*, 2016) model calibrated for the same data was used due to its enhanced flexibility in modelling small strain stiffness behaviour. In order to account for the increase in stiffness due to a reversal in loading direction, rather than simulating continuous degradation, the stiffness was reset to its maximum value every time such a change was anticipated (e.g. before the deposition of the superficial deposits, prior to the excavation of the WB tunnel, and prior to thermal operation – see Gawecka *et al.* (2017) for further considerations on the effect of resetting the stiffness in geotechnical problems involving thermal loading). It should also be noted that the angle of dilation of the Upper Lambeth Group was set to zero to avoid simulating excessive dilation during Stage 1, Stage 2 and the consolidation period in Stage 3 (Avgerinos *et al.*, 2018).

The London Clay units were modelled with the modified two-surface kinematic hardening model (M2-SKH, Grammatikopoulou *et al.*, 2006). The set of model parameters used in this study is the 'low triaxial' calibration, which was obtained by Avgerinos *et al.* (2016) based on the latest experimental data for London Clay (Gasparre, 2005; Hight *et al.*, 2007) and shown to predict well the short-term response of the ground due to tunnelling (Avgerinos *et al.*, 2016). This advanced constitutive model accounts automatically for changes in soil behaviour resulting from the recent stress history and the stress path direction. A brief description of the IC.G3S and M2-SKH models is provided in the Appendix.

The additional properties necessary for the THM stage of the analysis (i.e. coefficients of thermal expansion of the solid skeleton, α_s, and fluid, α_f, volumetric heat capacities, ρC_p, and thermal conductivities, k_T, listed in Table 7 in the Appendix) were adopted from Gawecka *et al.* (2017) who successfully reproduced the behaviour of a thermo-active pile installed in similar ground conditions to those featured in the current study. The permeability (k_T) of the consolidating materials was modelled as anisotropic with the profiles proposed by Avgerinos *et al.* (2018) shown in Figure 2 (a). Finally, the concrete tunnel linings were discretised using solid elements and modelled as linear-elastic.

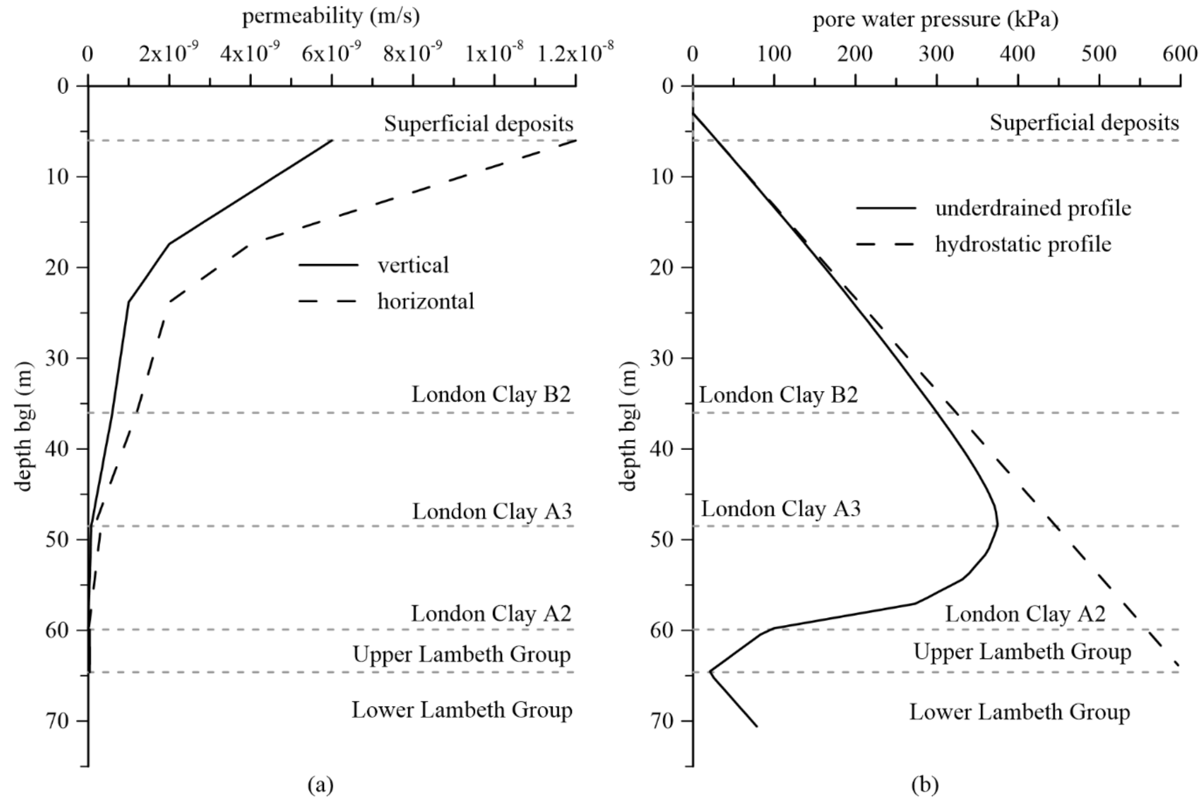

Figure 2 (a) permeability profile, (b) pore water pressure profiles in the finite element analyses

2.3.3 Initial conditions

The initial (i.e. prior to Stage 1) vertical effective stress profile was obtained from the unit weight values listed in Table 7 (see Appendix) assuming 180 m of overburden above the current top of the London Clay (i.e. the geological initial ground level), whereas the initial horizontal effective stresses were determined using K_0 values calculated from the Jaky (1948) expression (i.e. normally consolidated conditions) and the friction angles provided in Table 4 and Table 6 (see Appendix). The geological initial pore water pressure profile was assumed to be hydrostatic (Figure 2 (b)). The processes simulated in Stage 1 and Stage 2 resulted in the current overconsolidation of the clays and an underdrained pore water pressure profile (see Avgerinos *et al.*, 2018 and Figure 2 (b)) which are typical of the ground conditions in the London Basin and allow the realistic simulation of tunnelling effects. Lastly, the initial temperature across the finite element mesh was assumed to be 19.5 ˚C which is the ground temperature measured in the Lambeth College test (Bourne-Webb *et al.*, 2009) carried out at another London site with similar ground conditions.

2.3.4 Boundary conditions

The mechanical boundary conditions include no vertical or horizontal displacements ($u_x = u_y = 0$) at the bottom boundary of the mesh, and no horizontal displacements ($u_x = 0$) at the far left and right boundaries. The excavation of the tunnels was performed using the volume loss control method (Potts & Zdravković, 2001), with the tunnel lining being constructed as soon as the desired volume losses were reached (0.78 % and 1.39 % for the WB and EB tunnels, respectively). The procedure for determining the volume loss is explained in Avgerinos *et al.* (2018).

At the beginning of Stage 2 of the analysis, a pore water pressure of 19.62 kPa was prescribed at the interface between the Upper and Lower Lambeth Group in order to achieve the correct underdrained pore water pressure profile in the clay layers. This pore water pressure at the bottom of the Upper Lambeth Group, as well as that applied at the top of the London Clay (simulating the ground water level of 3 m bgl) were set to remain unchanged throughout Stages 2 to 6 ($\Delta p_f = 0$). As the superficial deposits and the Lower Lambeth Group were modelled as non-consolidating drained materials, the pore water pressure in these layers remained hydrostatic throughout the analysis. Following Stage 2, the pore water pressure at the far side boundaries of the mesh was not allowed to change ($\Delta p_f = 0$).

Avgerinos *et al.* (2018) demonstrated that the predicted response of the tunnel and the surrounding soil depends significantly on the permeability of the tunnel lining. Therefore, in this study, the two extreme scenarios of a fully permeable and a fully impermeable tunnel lining were considered. The fully permeable lining was modelled by prescribing a precipitation boundary condition (Potts & Zdravković, 1999) at the interface between the soil and the concrete lining. This is a dual boundary condition which sets either a zero pore water pressure or a zero water flow boundary condition on the selected nodes depending on whether the analysis computes water flow into or out of the excavated tunnel, respectively, with the change being picked up automatically by the software. Conversely, the fully impermeable lining was simulated with a no water flow boundary condition ($q_f = 0$) at the soil-lining interface.

In Stage 6 of the analysis (i.e. the coupled THM analysis) thermal boundary conditions must also be specified. At all mesh boundaries, the temperature was assumed to remain unchanged from the initial value ($\Delta T = 0$). The thermal load resulting from the thermal operation of the WB tunnel was modelled by prescribing a uniform temperature change of 15 ˚C (ΔT =15 ˚C) to all nodes of the tunnel lining. This simplified form of applying a thermal load, which has been used widely in the analysis of thermo-active structures (e,g, Rotta Loria *et al.*, 2015; Di Donna *et al.*, 2016; Rammal *et al.*, 2020), is adopted in this study to enable a clearer interpretation of the complex THM phenomena taking place within the surrounding soil. In order to simulate a more realistic start of the operation, the lining temperature was changed linearly over one month (i.e. at a rate of 0.5 ˚C per day) and then was kept constant for the remainder of the analysis. This final temperature (i.e. ±15 ˚C from initial temperature) was maintained for a total period of three years, which, despite being an extreme case of thermal operation of a thermo-active structure, provides more comprehensive information on the fundamental nature of the coupled phenomena taking place in the soil than more realistic operation patterns (e.g. balanced injection and extraction of heat).

Lastly, the coupled thermo-hydraulic boundary condition, which applies a heat flux equivalent to the energy associated with the flow of a fluid across a boundary (Cui *et al.*, 2016), was prescribed where water may leave or enter the mesh, i.e. the top of London Clay, the bottom of the Upper Lambeth Group, and the soil-tunnel lining interface. In the case of an impermeable, non-thermo-active tunnel (i.e. the EB tunnel), a no heat flux boundary condition ($q_T = 0$) was applied at the soil-tunnel lining interface.

2.4 Analyses performed

In order to explore the coupled THM interactions between the thermo-active tunnels and the surrounding soil, several analyses were performed for Stage 6. These analyses not only help understand the coupled mechanisms involved, but also allow the study of the effects of the chosen modelling approach in terms of the type of the FE analysis and permeability of the tunnel lining. All analyses presented in this paper are summarised in Table 2.

Analysis A can be considered as the baseline analysis with the results of other simulations being compared to those produced by Analysis A. It is a fully coupled THM analysis where the difference between the coefficients of thermal expansion of the soil skeleton and pore water (see Table 7 in the Appendix) leads to the generation of excess pore water pressures upon a temperature change. The numerical modelling of this phenomenon is explained in detail in Cui *et al.* (2018) and Cui *et al.* (2020). In this case, both tunnels are modelled as impermeable.

Analyses B1-B3 are termed 'undrained' as the soil permeability was set to an extremely small value such that there is no dissipation of excess pore water pressures due to consolidation/swelling. In these analyses, the modelling approach is changed in order to separate the different mechanics involved in a coupled THM behaviour. In Analyses B1, while water pressure generation due to both mechanical deformation and the differences in the thermal expansion coefficients of the water and soil skeleton is modelled, the effect of seepage is neglected. Subsequently, in Analysis B2 the generation of excess pore water pressures due to the difference in the thermal expansion coefficients of the soil skeleton and pore water is removed by setting these properties to the same value. However, it should be noted that excess pore water pressures resulting from mechanical deformation are still computed. Lastly, the modelling approach was simplified even further in Analysis B3 by neglecting the heat transfer through the soil and hence removing all time-dependent phenomena.

Analysis C is a fully coupled THM analysis where the tunnels were modelled as fully permeable and therefore its results will be compared to those of Analysis A to investigate the effect of lining permeability.

As part of this study, both energy extraction and energy injection through the tunnels were considered, and hence, the analyses listed in Table 2 were performed twice. In the case of the energy extraction mode, the temperature of the tunnel lining was reduced by 15 ˚C as explained before, whereas to simulate the energy injection mode, the temperature of the tunnel lining was increased by 15 ˚C. However, due to the length of the paper and the “symmetry” in the results (i.e. the magnitude of tensile forces induced by temperature reduction being similar to the magnitude of compressive forces due to an increase in temperature, etc.), only the former scenario (i.e. energy extraction) is discussed in the following sections.

Table 2 List of Stage 6 analyses performed

Analysis	Analysis type	Tunnel lining type
A	Coupled THM	Impermeable
B1	Undrained	Impermeable
B2	Undrained with $\alpha_f = \alpha_s$	Impermeable
B3	Undrained without heat transfer	Impermeable
C	Coupled THM	Permeable

3 Results and discussion

This section presents and explains the results of Stage 6 of the analyses described in the previous section. It should be noted that quantities termed ‘thermally-induced’ were computed by subtracting the solution at the beginning of Stage 6 from the current solution and, hence, represent the changes caused by variations in the temperature during the thermal operation of the tunnels. The sign convention adopted in this section is such that compressive forces, stresses and strains, as well as upward and rightward displacements are considered positive.

3.1 Behaviour of a thermo-active tunnel

Analysis A is a fully coupled THM analysis simulating cooling of the WB tunnel for a period of three years with both WB and EB tunnel linings assumed to be impermeable. Figure 3 shows the ground temperature after one month, six months, one year and three years of thermal operation. Naturally, as time goes on and energy is extracted from the ground, the volume of soil experiencing a reduction in temperature increases. The cooling of the tunnel and the ground causes their contraction which results in the increasing settlement of the ground surface plotted in Figure 4. The maximum thermally-induced surface settlement occurs at the tunnel axis and reaches values of 0.8 mm, 3.5 mm, 4.9 mm and 6.5 mm after one month, six months, one year and three years, respectively. The surface vertical displacement at the end of construction of the WB tunnel (Stage 3) is also plotted for comparison and it can be observed that the magnitude of the thermally-induced settlement is comparable to that due to construction of the tunnel, with the two matching after 13 months of continuous thermal operation (implying the total settlement to be approximately double the construction settlement). Lastly, the width of the settlement trough, and therefore the ground surface area affected by thermal operation, increases with time as the soil continues to cool down. However, it should be noted that the analyses assume a continuous heat extraction mode for an extended period of time, whereas a more realistic operation mode would involve both heat injection and extraction.

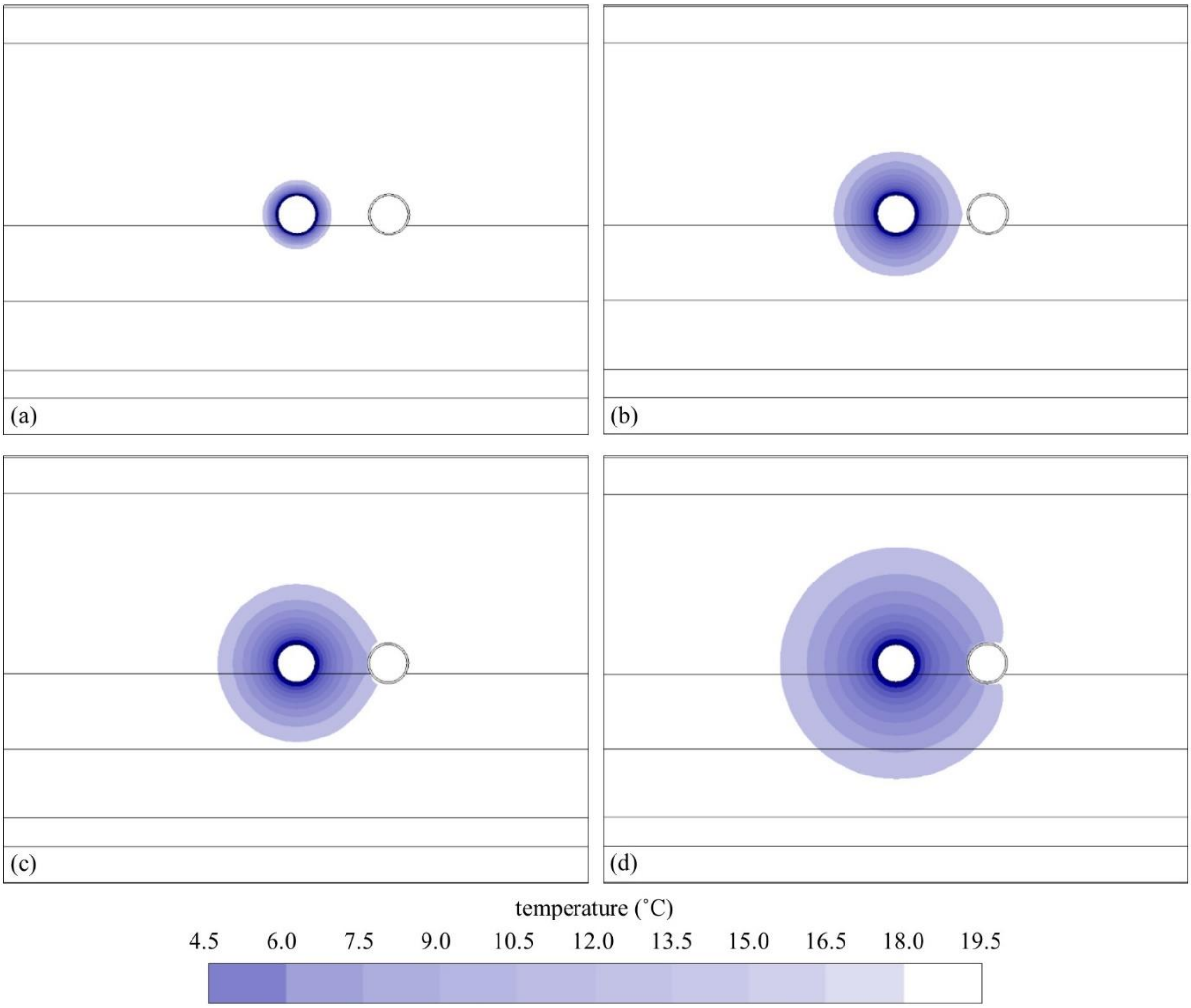

Figure 3 Temperature in Analysis A after: (a) 1 month, (b) 6 months, (c) 1 year, (d) 3 years

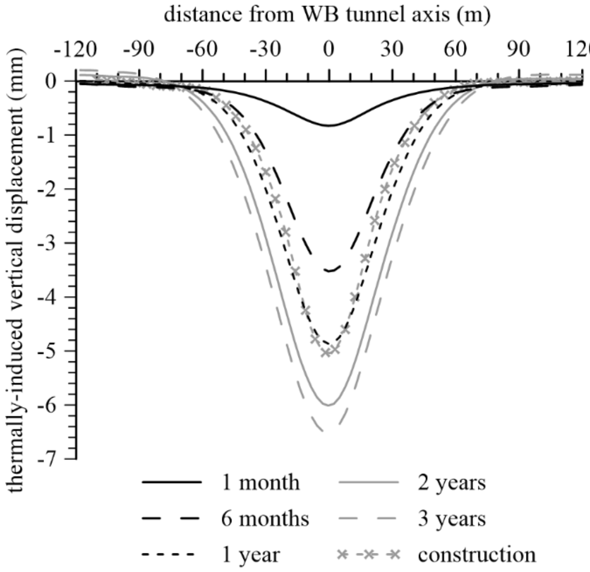

Figure 4 Thermally-induced surface vertical displacement in Analysis A

The thermally-induced deformation of the WB tunnel lining itself is illustrated in Figure 5 which shows (a) the vertical convergence of the crown and the invert, and the horizontal convergence along the springline, as well as (b) the deformed shape. Note that the latter is exaggerated for clarity. When the tunnel lining is cooled, it contracts, and hence, the convergence along both the vertical and horizontal axes is positive. Moreover, it is interesting to note that the lining contracts more in the vertical direction than along the springline resulting in an oval deformed shape. This is caused by the variation of soil stiffness around the tunnel due to the combination of the previous stress history and the applied stress path during excavation of the tunnel, with the soil around the springline undergoing vertical compression and the areas around the crown and invert experiencing extension.

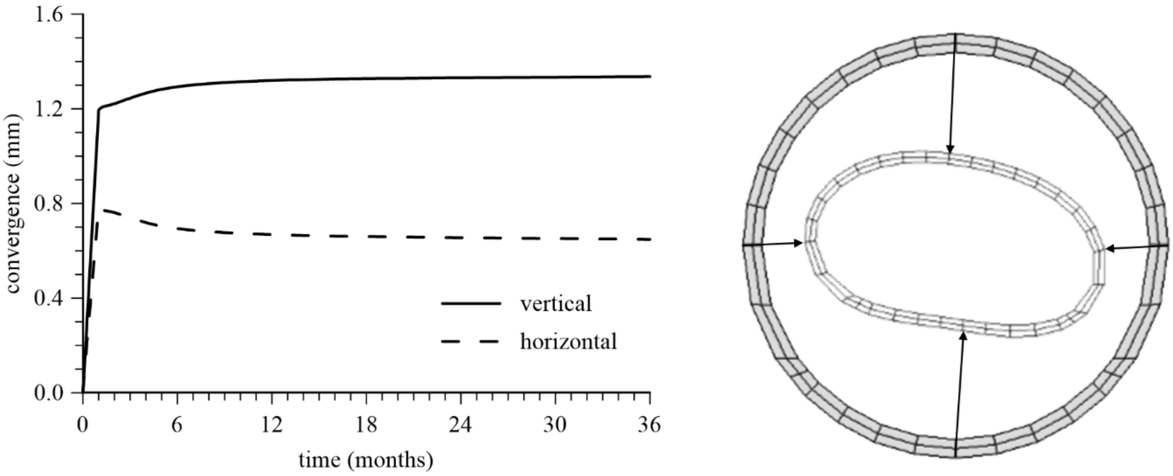

(a) (b)

Figure 5 Thermally-induced WB tunnel lining deformation in Analysis A: (a) horizontal and vertical axis convergence, (b) deformed shape after 1 year (exaggeration factor: 3000)

The thermal operation of the tunnel also results in changes in forces within the tunnel lining. Figure 6 plots the evolution of the thermally-induced axial force, showing that a tensile thermally-induced force (i.e. a reduction in the total axial force) was observed immediately after the start of the thermal operation. While the tunnel lining tends to contract due to the imposed temperature change, the surrounding soil provides a restraint to this movement which creates a tensile change in the axial force. It should be noted that, although there is a reduction in the normal stress at the soil-lining interface, the total stress remains compressive throughout the thermal operation. As time progresses and the soil around the tunnel cools down, the restriction to the tunnel lining’s movement reduces and, hence, the magnitude of the tensile thermally-induced axial force decreases as shown in Figure 6. This transient phenomenon has also been observed in thermo-active piles (Gawecka *et al.*, 2017) and thermo-active retaining walls (Sailer *et al.*, 2019). It must be noted that the magnitude of the thermally-induced axial forces (i.e. maximum of 27 kN/m) is very small compared to the total axial force which developed in the lining due to tunnel construction (i.e. approximately 2100 kN/m). The maximum (i.e. prior to thermal operation) and the minimum (i.e. after one month of cooling) total axial forces are plotted in Figure 7. These results suggest that the critical aspect of the behaviour of this thermo-active tunnel relates to the deformation of the lining and the surrounding soil, rather than excessive force changes in the lining. Nonetheless, it is interesting to point out that the springline of the tunnel (i.e. θ of 0˚ and 180˚) experiences the largest compressive total axial force and the smallest tensile thermally-induced axial force, whereas the smallest compressive total axial force and the largest tensile thermally-induced axial force occur at the tunnel crown and invert (i.e. θ of 90˚ and 270˚) in accordance with the deformation of the lining. The bending moments generated within the tunnel lining due to temperature changes range from -5 to +6 kNm/m, being about 10% of those due to the construction of the tunnel (ranging from -60 to +70 kNm/m).

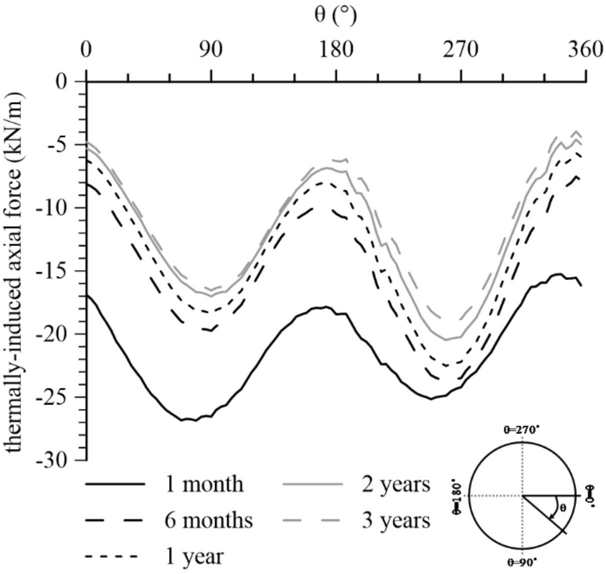

Figure 6 Thermally-induced axial force in WB tunnel lining in Analysis A

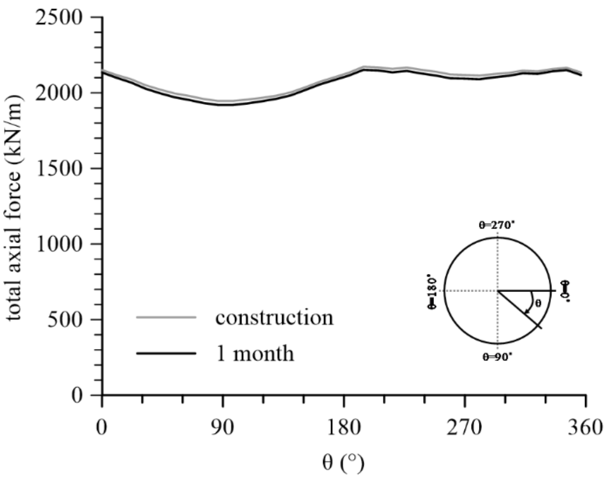

Figure 7 Total axial force in WB tunnel lining in Analysis A

During the thermal operation, the pore water pressure in the surrounding soil changes due the difference in the thermal expansion coefficient of soil skeleton and pore water, as well as due to the deformation of the tunnel lining and the soil. These thermally-induced pore water pressures are presented in Figure 8. When the temperature in the soil reduces, and the soil and the tunnel contract, tensile changes in pore water pressure are generated around the tunnel (see Cui *et al.*, 2020 for further discussions on thermally-induced pore water pressures). While these tensile thermally-induced pore water pressures adjacent to the tunnel lining dissipate with time, the radius of influence around the tunnel increases as a greater volume of the soil experiences a temperature decrease. It is interesting to point out the oval spatial distribution of the thermally-induced pore water pressures caused by the anisotropic permeability of the clay layers where the horizontal permeability is larger than the vertical. However, it should be noted that the magnitude of the pore water pressure changes is relatively small.

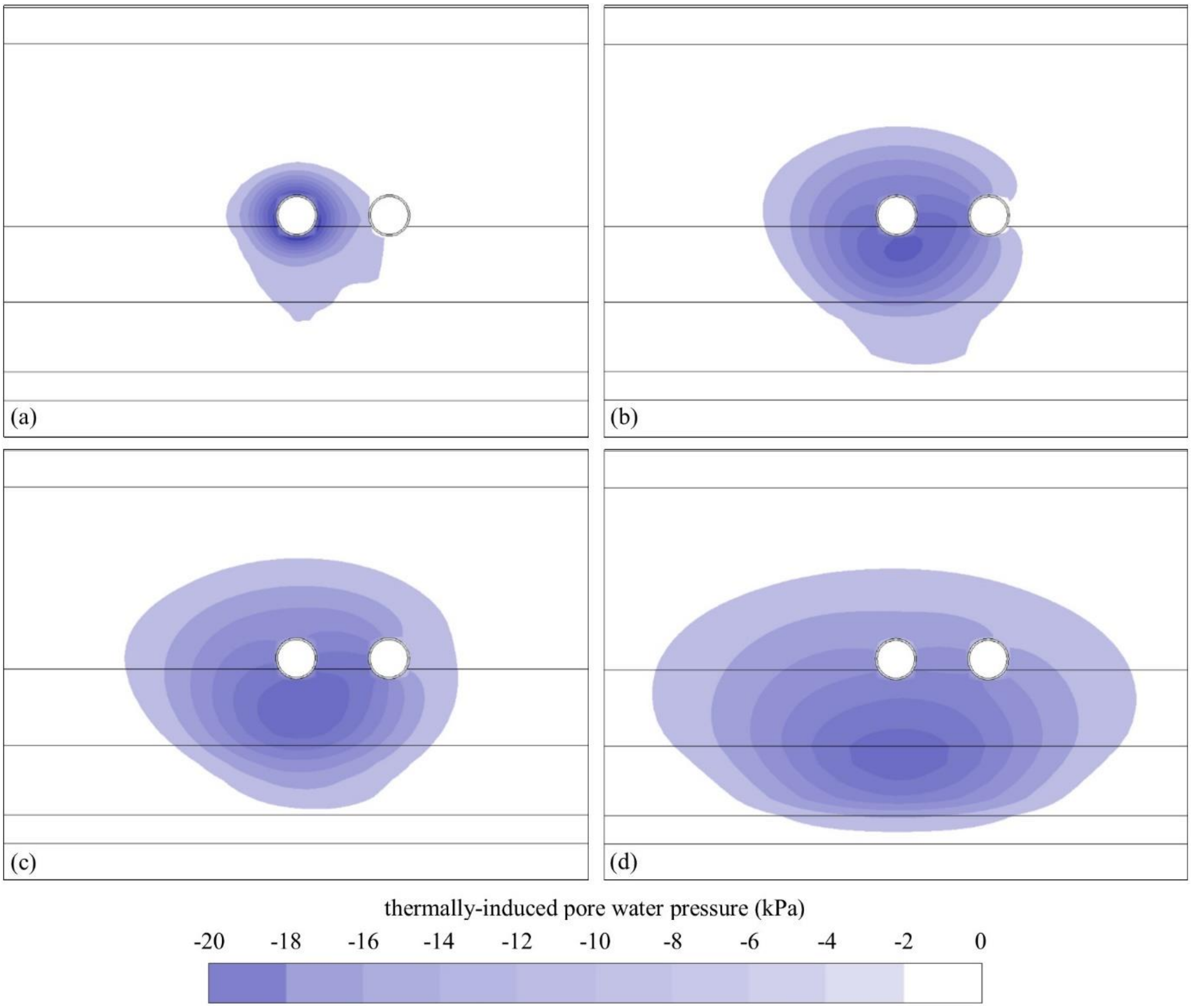

Figure 8 Thermally-induced pore water pressure in Analysis A after: (a) 1 month, (b) 6 months, (c) 1 year, (d) 3 years

3.2 Behaviour of an adjacent non-thermo-active tunnel

In addition to understanding the behaviour of a thermo-active tunnel, it is also important to consider the effects it has on any adjacent tunnels which may not be used for energy exchange. This section discusses the response of the EB tunnel in Analysis A which was modelled as non-thermo-active.

Figure 9 compares the deformation of the two tunnels in Analysis A after one year of thermal operation. Note that the magnitude of the deformation in Figure 9 (b) and (c) is exaggerated in order to highlight the deformed shape. While the WB tunnel contracts due to the imposed temperature change and hence its cross-sectional area reduces, the cross-sectional area of the EB tunnel remains relatively unchanged with values of convergence along the vertical and horizontal axes having approximately equal magnitudes but opposite signs. However, as the WB tunnel and the surrounding soil contract, the EB tunnel extends in the horizontal direction resulting in an oval deformed shape. It is interesting to note that the magnitude of deformation of the two tunnels is similar, despite only the WB tunnel being thermally active and only a very small temperature change reaching to the EB tunnel (an average of 3.2 ˚C change around the tunnel perimeter, with values reaching 6.43 ˚C at the springline on the side facing the WB tunnel, but limited to 0.97 ˚C on the opposite side).

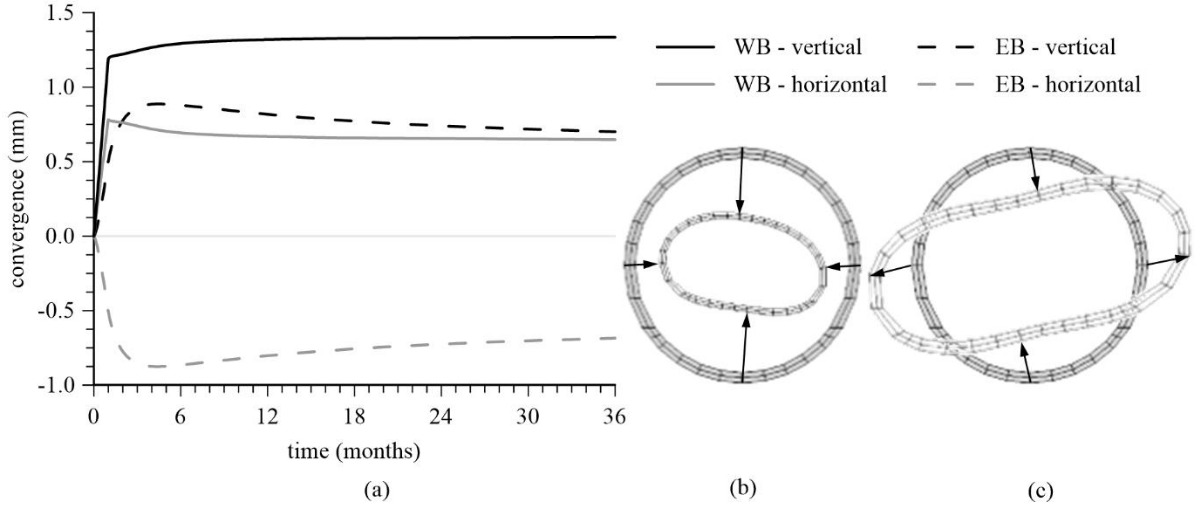

Figure 9 Thermally-induced tunnel lining deformations in Analysis A: (a) horizontal and vertical axis convergence of WB and EB tunnels, (b) deformed shape of WB tunnel after 1 year (exaggeration factor: 3000), (c) deformed shape of EB tunnel after 1 year (exaggeration factor: 3000)

The thermally-induced axial force in the EB tunnel lining is plotted in Figure 10. Unlike the WB tunnel which experiences only tensile thermally-induced axial forces, the EB tunnel carries both tensile and compressive changes in axial force. The distribution of these thermally-induced axial forces along the perimeter is linked to the tunnel's deformation. As the tunnel is extended in the horizontal direction, the areas around the crown and invert (i.e. θ of 90˚ and 270˚) experience a tensile change in axial force, whereas the areas around the springline (i.e. θ of 0˚ and 180˚) show a compressive change. The magnitude of these thermally-induced axial forces tends to increase with time as the EB tunnel continues to deform. It is interesting to note that the magnitudes of the change in axial force is similar to that in the WB tunnel, suggesting that the thermal operation of one tunnel has an equal effect on the adjacent non-thermo-active tunnel compared to that on itself. Finally, the thermally-induced bending moments in the EB tunnel lining vary from -12 to +13 kNm/m which constitutes approximately 20% change from the bending moments generated during the construction (ranging from -70 to +60 kNm/m) and over twice the thermally-induced bending moments in the WB tunnel lining.

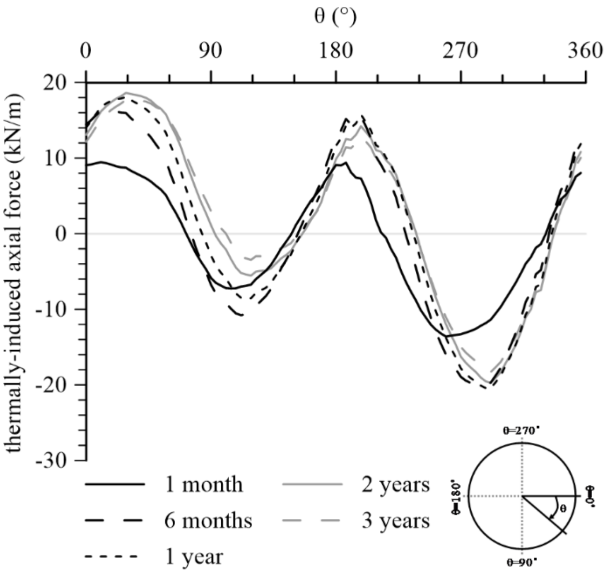

Figure 10 Thermally-induced axial force in EB tunnel lining in Analysis A

3.3 Coupled THM interactions

Analyses B1-B3 were performed in order to illustrate and explain the complex coupled THM interactions observed in Analysis A. This was achieved by adopting different simplified modelling approaches which remove some of the aspects of the coupled THM soil behaviour. These coupled THM interactions are best explained by considering the evolutions of thermally-induced pore water pressures plotted in Figure 11 for the position 0.6 m below the invert of the tunnel, and the evolutions of the maximum thermally-induced ground vertical displacements above the WB tunnel presented in Figure 12. Note that the latter quantity represents the largest ground movement along the WB tunnel vertical axis, between the crown and the ground surface, at any time instant. For clarity, only the results of the first year of thermal operation are presented.

The smallest pore water pressure and vertical displacement changes are observed in Analysis B3 where neither pore water pressure dissipation nor heat transfer within the soil were modelled, thus simulating a time-independent response during the period over which the tunnel lining temperature was kept constant (i.e. from the end of the first month). Clearly, the contraction of the tunnel lining and the resulting tensile deformation of the surrounding soil lead to a small tensile thermally-induced pore water pressure and downward ground movement.

Analysis B2 accounted for the transient heat transfer within the soil, although the thermal expansion coefficient of pore water was chosen to be the same as that of the soil skeleton, such that no pore water pressure change due to their difference was generated (Cui *et al.*, 2018; Cui *et al.*, 2020). Hence, the tensile thermally-induced pore water pressure and the downward ground movement are caused only by the thermal contraction of the tunnel lining and the soil, where the latter increases in magnitude with time as the surrounding soil gradually cools down and contracts. As no pore pressure dissipation was allowed in Analysis B2 or Analysis B3, the significant difference in the results is due to the thermal contraction of the soil surrounding the tunnel which is simulated in the former but not in the latter.

Analysis B1 differs from Analysis B2 only by the thermal expansion coefficient of the pore water which is greater than that of the soil skeleton (see Table 7 in the Appendix). By comparing the results of analysis B1 and B2, it can be observed that a much larger tensile thermally-induced pore water pressure was computed in the former due to the greater changes in volume modelled for the water phase. This additional reduction in pore water pressure further increases the effective stress in the soil, resulting in further contraction of the soil, and hence additional vertical displacements in Analysis B1, as shown in Figure 12.

Analyses B1, B2 and B3 are termed "undrained" as the process of dissipation of pore water was neglected, whereas Analysis A is a fully coupled THM analysis where the soils have a finite permeability, the results of which were discussed in detail in Sections 3.1 and 3.2. Hence, the final comparison of analyses A and B1 demonstrates the effect of dissipation of excess pore water pressures with time. In effect, the difference between the thermally-induced pore water pressures in analyses A and B1 observed in Figure 11 represents the amount of tensile pore water pressures which were dissipated in the former. Naturally, this process leads to swelling of the soil resulting in its smaller overall contraction and smaller downward ground movement than that observed in Analysis B1, as illustrated in Figure 12.

The results presented here clearly demonstrate the importance of the chosen modelling approach and its effect on the computed displacements and pore water pressures. For example, assuming that the soil behaves in an undrained manner and neglecting the process of dissipation of excess pore water pressures as in Analysis B1 is conservative, overestimating the ground movements. Conversely, the simplest, yet commonly used (e.g. Ozudogru *et al.*, 2015; Ng *et al.*, 2016), approach of modelling the soil as undrained and thermally inert (Analysis B3) is unconservative, significantly underestimating the ground settlements.

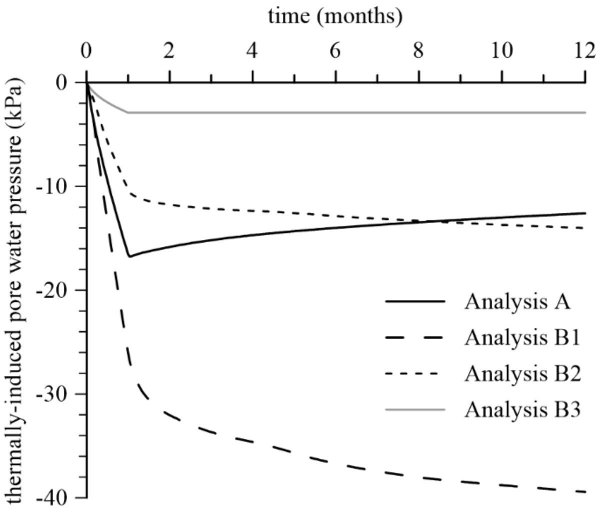

Figure 11 Thermally-induced pore water pressure 0.6 m below WB tunnel in analyses A, B1, B2 and B3

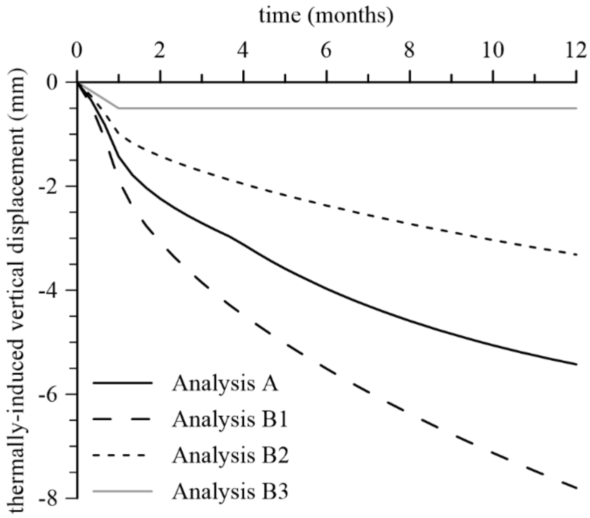

Figure 12 Maximum thermally-induced ground vertical displacement above WB tunnel in analyses A, B1, B2 and B3

Lastly, Figure 13 plots the evolution of the largest tensile thermally-induced axial force in the tunnel lining observed at any time instant. Again, the effect of thermal operation on the axial force is limited compared to the axial force generated during tunnel excavation, with analyses A, B2 and B3 showing similar trends. The tensile thermally-induced forces computed in Analysis B1 are slightly larger due to a much greater contraction of the soil mass around the tunnel (see Figure 12). A similar conclusion can be drawn for the bending moment variation.

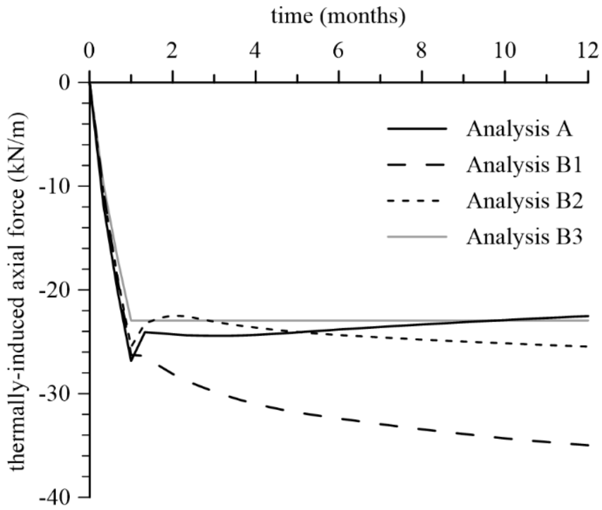

Figure 13 Maximum thermally-induced axial force in WB tunnel lining in analyses A, B1, B2 and B3

3.4 Effect of tunnel lining permeability

Avgerinos *et al.* (2018) showed that tunnel permeability has a significant effect on its response during construction, as well as in the short-term post construction. As part of this study, the effect of the tunnel lining permeability was investigated by comparing the results of Analysis A, where the lining was modelled as impermeable, and Analysis C where a fully permeable lining is simulated. It should be noted that both analyses are fully THM coupled.

Figure 14 compares the evolution of the thermally-induced pore water pressure in the two analyses. Due to shorter drainage paths created by the permeable tunnel lining, excess pore water pressure dissipation is much faster in Analysis C and, hence, the observed tensile thermally-induced pore water pressures are smaller. It is interesting to note that such tensile pore water pressures are not large enough to overcome the initially compressive pore water pressure observed at the start of the thermal operation. Therefore, in these conditions, the dual boundary condition used (see section 2.3.4) sets a zero pore water pressure condition along the tunnel-soil interface, allowing further drainage of water into the tunnel. As a result, further dissipation of the generated thermally-induced tensile pore water pressures leads to greater swelling of the soil, and hence to its smaller overall contraction, which is illustrated by the smaller downward movements in Analysis C shown in Figure 15.

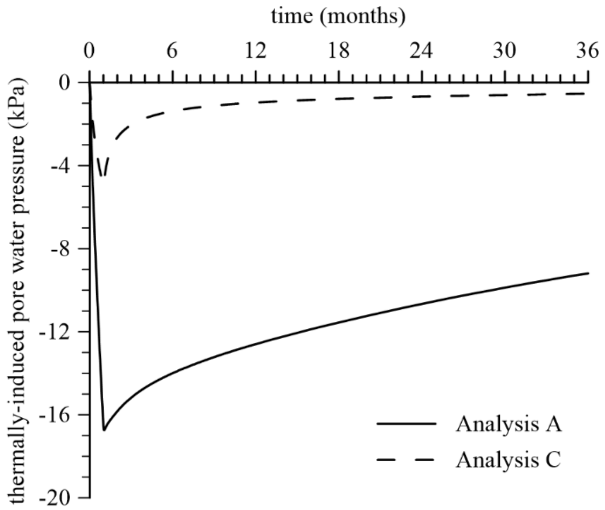

Figure 14 Thermally-induced pore water pressure 0.6 m below WB tunnel in analyses A and C

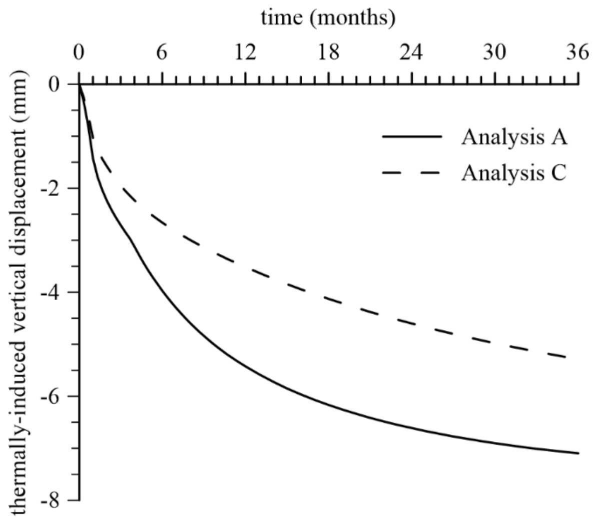

Figure 15 Maximum thermally-induced ground vertical displacement above WB tunnel in analyses A and C

The deformation of the tunnel lining is also different depending on its permeability, as shown in Figure 16 which plots the convergence between the crown and invert, and along the springline, as well as the exaggerated deformed shapes. While the impermeable tunnel contracts more along the vertical axis than the horizontal axis, the opposite is true for the permeable tunnel. As the excess pore water pressures dissipate faster in Analysis C, the soil around the tunnel swells more (see Figure 14 and Figure 15). Furthermore, due to the anisotropic soil permeability, the rates of excess pore water pressure dissipation and swelling are greater in the horizontal direction, causing a larger compression of the tunnel lining along the horizontal axis. Lastly, the effect of the permeability of the tunnel lining on the maximum magnitude of the thermally-induced forces in the lining appeared to be relatively small, both in terms of axial force and bending moment.

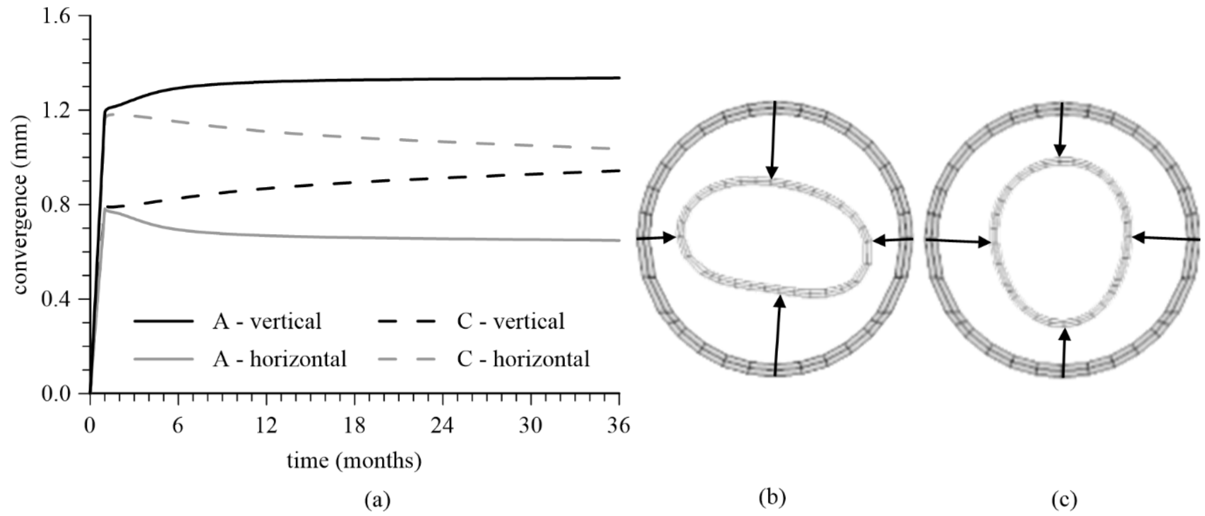

Figure 16 Thermally-induced WB tunnel lining deformation: (a) horizontal and vertical axis convergence in analyses A and C, (b) deformed shape after 1 year in Analysis A (exaggeration factor: 3000), (c) deformed shape after 1 year in Analysis C (exaggeration factor: 3000)

4 Conclusions

This paper presents a comprehensive numerical study which investigates the coupled THM interactions between thermo-active tunnels and the surrounding soil. An extreme operation mode – continuous heat extraction or injection for three years – enabled the detailed study of the complex soil-structure interaction phenomena induced by this type of structures and, hence, the observed behaviour in terms of forces and displacements needs to be considered within this context. Realistic features of the ground conditions are taken into account in the FE model, which is an extension of the model developed by Avgerinos *et al.* (2018) that had successfully reproduced the isothermal response of the Crossrail tunnels at Hyde Park in London, UK. The main conclusions that arise from this study are:

(1) The fully coupled THM analysis of a tunnel used for continuous energy extraction showed that cooling and contraction of both the tunnel lining and the surrounding soil results in significant ground deformations, with the thermally-induced ground surface settlements after one year of operation being similar to those measured during tunnel construction.

(2) The thermally-induced deformation of the tunnel lining was observed to be non-uniform along the perimeter, producing an oval deformed shape. The associated changes in axial force in the lining were found to be relatively small compared to those due to tunnel construction. However, the changes in bending moment were of the order of 10% of those existing after construction. In effect, it is the thermally-induced displacements that are likely to be critical in future design criteria.

(3) The analysis further demonstrated that the deformations and structural forces in the adjacent non-thermo-active tunnel were comparable to those in the thermo-active one, indicating a strong interaction between the two tunnels.

(4) In exploring the coupled THM interactions between the thermo-active tunnel and the surrounding soil, the study demonstrated that the commonly used approach of only considering the effect of temperature change on the lining (i.e. neglecting heat transfer) leads to grossly unconservative predictions. This is in agreement with studies performed on other thermo-active structures, such as piles (Gawecka *et al.*, 2017) and retaining walls (Sailer *et al.*, 2019). Conversely, neglecting the dissipation of excess pore water pressures leads to an overestimation of the ground movements. The fully coupled THM analyses reproduce the soil behaviour most accurately.

(5) The final set of analyses showed that the effect of tunnel lining permeability is also significant. A fully permeable tunnel lining allows a quicker dissipation of the tensile thermally-induced pore water pressures. It causes the soil to swell more which reduces the effect of contraction due to cooling and results in smaller thermally-induced ground settlements.

Although the present study considers a hypothetical scenario where one of the Crossrail tunnels is thermo-active, it represents the behaviour of a thermo-active tunnel constructed in ground conditions typical of the London Basin and, hence, serves as an example for future tunnelling projects in London and other stiff clay sites.

Acknowledgements

The research presented in this paper was partly funded by the Geotechnical Consulting Group (GCG, UK). The authors wish to thank Dr Vasilis Avgerinos for his support on modelling isothermal soil-tunnel interactions.

Appendix

Material properties

Table 3 Linear elastic material properties

Material	E (kPa)	μ
Superficial deposits	10×10^3	0.30
Concrete	40×10^6	0.15

Table 4 Mohr-Coulomb strength properties

Material	c' (kPa)	φ' (°)	ψ' (°)
Superficial deposits	0.0	25.0	12.5
Upper Lambeth Group	0.0	28.0	14.0
Lower Lambeth Group	0.0	36.0	18.0

Table 5 IC.G3S model properties

Material	G_{ref} (kPa)	a	b	$R_{G,min}$ (kPa)	G_{min} (kPa)
Upper Lambeth Group	33456.8	0.000112	1.2688	0.0670	2000
Lower Lambeth Group	37717.4	0.000095	1.0447	0.0930	2000
Material	K_{ref} (kPa)	r	s	$R_{K,min}$ (kPa)	K_{min} (kPa)
Upper Lambeth Group	30011.2	0.000065	1.1260	0.0964	2500
Lower Lambeth Group	44975.0	0.000244	1.1427	0.0860	2500

Note: p'_{ref} = 100 kPa, m_G = 1.0, m_K = 1.0 for all strata

Table 6 M2-SKH model parameters

Material	ν_1	λ	κ	n	m	A_1	φ' (°)	R	A_2
London Clay B2	2.50	0.12	0.060	0.87	0.28	250	25.0	0.010	0.8
London Clay A3 & A2	2.75	0.15	0.063	0.87	0.28	180	20.3	0.005	0.8

Table 7 Thermal and thermo-mechanical properties

Material	γ_s (kN/m^3)	α_s (m/mK)	α_f (m/mK)	K_f (kPa)	ρC_p (kJ/m^{3}K)	k_T (kW/mK)
Superficial deposits	18	1.7×10^{-5}	-	-	1900	1.40×10^{-3}
London Clay	20	1.7×10^{-5}	6.9×10^{-5}	2.2×10^{6}	1820	1.79×10^{-3}
Lambeth Group	20	1.7×10^{-5}	6.9×10^{-5}	2.2×10^{6}	1760	2.20×10^{-3}
Concrete	30	8.5×10^{-6}	-	-	-	-

IC.G3S model

The maximum shear and bulk moduli are defined as:

$$G_{max} = G_{ref}\left(\frac{p'}{p'_{ref}}\right)^{m_G} \tag{1}$$

$$K_{max} = K_{ref}\left(\frac{p'}{p'_{ref}}\right)^{m_K} \tag{2}$$

where the parameters m_G and m_K control the non-linearity of the stiffness dependency on the mean effective stress.

The degradation of the tangent shear and bulk moduli are calculated using:

$$G_{tan} = G_{max}\left(R_{G,min} + \frac{1 - R_{G,min}}{1 + (E_d/a)^b}\right) \tag{3}$$

$$K_{tan} = K_{max}\left(R_{K,min} + \frac{1 - R_{K,min}}{1 + (|\varepsilon_{vol}|/r)^s}\right) \quad (4)$$

The strain invariants are defined as:

$$E_d = \frac{2}{\sqrt{6}}\sqrt{(\varepsilon_1 - \varepsilon_2)^2 + (\varepsilon_2 - \varepsilon_3)^2 + (\varepsilon_3 - \varepsilon_1)^2} \quad (5)$$

$$\varepsilon_{vol} = \varepsilon_1 + \varepsilon_2 + \varepsilon_3 \quad (6)$$

M2-SKH model

The M2-SKH is a modified version of the model proposed by Al-Tabbaa & Wood (1989) and its formulation is described in detail in Grammatikopoulou (2004) and Grammatikopoulou *et al.* (2006). It adopts the elliptical shape of the Modified Cam-Clay (Roscoe & Burland, 1968) as the bounding surface, which delimits the stress space within which the yield surface can move. This yield surface has the same shape as the bounding surface but is of a much smaller size, hence the common designation of ‘bubble’. In this version of the model, the ratio between the size of the bounding and yield surfaces remains constant, meaning that there is isotropic (i.e. when the bounding surface expands or contracts, so does the yield surface) as well as kinematic hardening. Within the elastic region delimited by the small yield surface, the behaviour of the material is described by a constant Poisson’s ratio and the non-linear elastic formulation for the bulk stiffness arising from the assumption of swelling lines of constant slope in $\nu - \ln p'$ space:

$$K = \frac{\nu p'}{\kappa} \quad (7)$$

References

Adam, D. & Markiewicz, R. (2009) Energy from earth-coupled structures, foundations, tunnels and sewers. *Geotechnique*. 59 (3), 229–236. Available from: 10.1680/geot.2009.59.3.229.

Al-Tabbaa, A. & Wood, D. M. (1989) An experimentally based "bubble' model for clay. In: Pietruszak, A. & Pande, G. N. (eds.) *Proceedings of international conference on numerical models in geomechanics.* Rotterdam, Balkema, 91–99.

Avgerinos, V., Potts, D. M. & Standing, J. R. (2016) The use of kinematic hardening models for predicting tunnelling-induced ground movements in London Clay. *Géotechnique*. 66 (2), 106–120. Available from: 10.1680/jgeot.15.P.035.

Avgerinos, V., Potts, D. M., Standing, J. R. & Wan, M. S. P. (2018) Predicting tunnelling-induced ground movements and interpreting field measurements using numerical analysis: Crossrail case study at Hyde Park. *Géotechnique*. 68 (1), 31–49. Available from: 10.1680/jgeot.16.P.219.

Banks, D. (2012) *An Introduction to Thermogeology: Ground Source Heating and Cooling*. 2nd ed. Chichester, Wiley-Blackwell.

Baralis, M., Barla, M., Bogusz, W., Di Donna, A., Ryżyński, G. & Żeruń, M. (2018) Geothermal potential of the NE extension Warsaw (Poland) metro tunnels. *Proceedings of the Institution of Civil Engineers - Environmental Geotechnics*. Available from: 10.1680/jenge.18.00042.

Barla, M. & Di Donna, A. (2018) Energy tunnels: concept and design aspects. *Underground Space*. 3 (4), 268–276. Available from: 10.1016/j.undsp.2018.03.003.

Barla, M., Di Donna, A. & Insana, A. (2019) A novel real-scale experimental prototype of energy tunnel. *Tunnelling and Underground Space Technology*. 87, 1–14. Available from: 10.1016/j.tust.2019.01.024.

Barla, M., Di Donna, A. & Perino, A. (2016) Application of energy tunnels to an urban environment. *Geothermics*. 61, 104–113. Available from: 10.1016/j.geothermics.2016.01.014.

Bidarmaghz, A. & Narsilio, G. A. (2018) Heat exchange mechanisms in energy tunnel systems. *Geomechanics for Energy and the Environment*. 16, 83–95. Available from: 10.1016/j.gete.2018.07.004.

Bidarmaghz, A., Narsilio, G. A., Buhmann, P., Moormann, C. & Westrich, B. (2017) Thermal interaction between tunnel ground heat exchangers and borehole heat exchangers. *Geomechanics for Energy and the Environment*. 10, 29–41. Available from: 10.1016/j.gete.2017.05.001.

Bourne-Webb, P. & Gonçalves, R. d. C. (2016) On the exploitation of ground heat using transportation infrastructure. *Procedia Engineering*. 143, 1333–1340. Available from: 10.1016/j.proeng.2016.06.157.

Bourne-Webb, P. J., Amatya, B., Soga, K., Amis, T., Davidson, C. & Payne, P. (2009) Energy pile test at Lambeth College, London: geotechnical and thermodynamic aspects of pile response to heat cycles. *Geotechnique*. 59 (3), 237–248. Available from: 10.1680/geot.2009.59.3.237.

Bourne-Webb, P. J., Bodas Freitas, T. M. & da Costa Gonçalves, R. A. (2016) Thermal and mechanical aspects of the response of embedded retaining walls used as shallow geothermal heat exchangers. *Energy and Buildings*. 125, 130–141. Available from: 10.1016/j.enbuild.2016.04.075.

Brandl, H. (2006) Energy foundations and other thermo-active ground structures. *Geotechnique*. 56 (2), 81–122. Available from: 10.1680/geot.2006.56.2.81.

Buhmann, P., Moormann, C. & Westrich, B. (2019) Angle of incidence on geothermal tunnel plants - a calculation concept. In: IGS (ed.) *Proceedings of the XVII European Conference on Soil Mechanics and Geotechnical Engineering.* Reykjavík, IGS. Available from: 10.32075/17ECSMGE-2019-0198.

Buhmann, P., Moormann, C., Westrich, B., Pralle, N. & Friedemann, W. (2016) Tunnel geothermics - A German experience with renewable energy concepts in tunnel projects. *Geomechanics for Energy and the Environment*. 8, 1–7. Available from: 10.1016/j.gete.2016.10.006.

Cui, W., Gawecka, K. A., Potts, D. M., Taborda, D. M. G. & Zdravković, L. (2016) Numerical analysis of coupled thermo-hydraulic problems in geotechnical engineering. *Geomechanics for Energy and the Environment*. 6, 22–34. Available from: 10.1016/j.gete.2016.03.002.

Cui, W., Potts, D. M., Zdravković, L., Gawecka, K. A. & Taborda, D. M. G. (2018) An alternative coupled thermo-hydro-mechanical finite element formulation for fully saturated soils. *Computers and Geotechnics*. 94, 22–30. Available from: 10.1016/j.compgeo.2017.08.011.

Cui, W., Tsiampousi, A., Potts, D. M., Gawecka, K. A. & Zdravković, L. (2020) Numerical modelling of time-dependent thermally induced excess pore fluid pressures in a saturated soil. *ASCE Journal of Geotechnical and Geoenvironmental Engineering*. 146 (4). Available from: 10.1061/(ASCE)GT.1943-5606.0002218.

Di Donna, A. & Barla, M. (2016) The role of ground conditions on energy tunnels' heat exchange. *Proceedings of the Institution of Civil Engineers - Environmental Geotechnics*. 3 (4), 214–224. Available from: 10.1680/jenge.15.00030.

Di Donna, A., Rotta Loria, A. F. & Laloui, L. (2016) Numerical study of the response of a group of energy piles under different combinations of thermo-mechanical loads. *Computers and Geotechnics*. 72, 126–142. Available from: 10.1016/j.compgeo.2015.11.010.

Franzius, J. N. & Pralle, N. (2011) Turning segmental tunnels into sources of renewable energy. *Proceedings of the Institution of Civil Engineers - Civil Engineering*. 164 (CE1), 35–40. Available from: 10.1680/cien.2011.164.1.35.

Gasparre, A. (2005) *Advanced Laboratory Characterisation of London Clay*. PhD. Imperial College London, UK.

Gawecka, K. A., Taborda, D. M. G., Potts, D. M., Cui, W., Zdravković, L. & Haji Kasri, M. S. (2017) Numerical modelling of thermo-active piles in London Clay. *Proceedings of the Institution of Civil Engineers - Geotechnical Engineering*. 170 (3), 201–219. Available from: 10.1680/jgeen.16.00096.

Grammatikopoulou, A. (2004) *Development, implementation and application of kinematic hardening models for overconsolidated clays*. PhD. Imperial College London.

Grammatikopoulou, A., Zdravkovic, L. & Potts, D. M. (2006) General Formulation of Two Kinematic Hardening Constitutive Models with a Smooth Elastoplastic Transition. *International Journal of Geomechanics*. 6 (5), 291–302. Available from: 10.1061/(ASCE)1532-3641(2006)6:5(291).

Hight, D. W., Gasparre, A., Nishimura, S., Minh, N. A., Jardine, R. J. & Coop, M. R. (2007) Characteristics of the London Clay from the Terminal 5 site at Heathrow Airport. *Géotechnique*. 57 (1), 3–18. Available from: 10.1680/geot.2007.57.1.3.

Jaky, J. (1948) Pressure in soils *Proceedings of the 2nd International Conference on Soil Mechanics and Foundation Engineering*, 103–107.

Jardine, R. J., Potts, D. M., Fourie, A. B. & Burland, J. B. (1986) Studies of the influence of non-linear stress–strain characteristics in soil–structure interaction. *Géotechnique*. 36 (3), 377–396. Available from: 10.1680/geot.1986.36.3.377.

King, C. (1981) *The stratigraphy of London Basin and associated deposits*. Rotterdam, Backhuys.

Laloui, L., Nuth, M. & Vulliet, L. (2006) Experimental and numerical investigations of the behaviour of a heat exchanger pile. *International Journal for Numerical and Analytical Methods in Geomechanics*. 30 (8), 763–781. Available from: 10.1002/nag.499.

Lee, C., Park, S., Won, J., Jeoung, J., Sohn, B. & Choi, H. (2012) Evaluation of thermal performance of energy textile installed in Tunnel. *Renewable Energy*. 42, 11–22.

Ng, C. W. W., Ma, Q. J. & Gunawan, A. (2016) Horizontal stress change of energy piles subjected to thermal cycles in sand. *Computers and Geotechnics*. 78, 54–61. Available from: 10.1016/j.compgeo.2016.05.003.

Nicholson, D. P., Chen, Q., Pillai, A. & Chendorain, M. (2013) Developments in thermal pile and thermal tunnel linings for city scale GSHP systems *Proceedings of the 38th Workshop on Geothermal Reservoir Engineering.* Stanford, USA, Stanford Geothermal Program.

Ozudogru, T. Y., Olgun, C. G. & Arson, C. F. (2015) Analysis of friction induced thermo-mechanical stresses on a heat exchanger pile in isothermal soil. *Geotechnical and Geological Engineering*. 33 (2), 357–371. Available from: 10.1007/s10706-014-9821-0.

Potts, D. M. & Zdravković, L. (1999) *Finite Element Analysis in Geotechnical Engineering: Theory*. London, Thomas Telford.

Potts, D. M. & Zdravković, L. (2001) *Finite Element Analysis in Geotechnical Engineering: Application*. London, Thomas Telford.

Rammal, D., Mroueh, H. & Burlon, S. (2020) Thermal behaviour of geothermal diaphragm walls: Evaluation of exchanged thermal power. *Renewable Energy*. 147, 2643–2653. Available from: 10.1016/j.renene.2018.11.068.

Roscoe, K. H. & Burland, J. B. (1968) On the generalized stress-strain behaviour of wet clay. *Engineering Plasticity*, 535–609.

Rotta Loria, A. F., Gunawan, A., Shi, C., Laloui, L. & Ng, C. W. W. (2015) Numerical modelling of energy piles in saturated sand subjected to thermo-mechanical loads. *Geomechanics for Energy and the Environment*. 1 (2015), 1–15. Available from: 10.1016/j.gete.2015.03.002.

Sailer, E., Taborda, D. M.G., Zdravković, L. & Potts, D. M. (2019) Fundamentals of the coupled thermo-hydro-mechanical behaviour of thermo-active retaining walls. *Computers and Geotechnics*. 109, 189–203. Available from: 10.1016/j.compgeo.2019.01.017.

Sterpi, D., Angelotti, A., Habibzadeh-Bigdarvish, O. & Jalili, D. (2018) Assessment of thermal behaviour of thermo-active diaphragm walls based on monitoring data. *Journal of Rock Mechanics and Geotechnical Engineering*. 10 (6), 1145–1153. Available from: 10.1016/j.jrmge.2018.08.002.

Taborda, D. M. G., Potts, D. M. & Zdravković, L. (2016) On the assessment of energy dissipated through hysteresis in finite element analysis. *Computers and Geotechnics*. 71, 180–194. Available from: 10.1016/j.compgeo.2015.09.001.

Wan, M. S. P. & Standing, J. R. (2014) Field measurement by fully grouted vibrating wire piezometers. *Proceedings of the Institution of Civil Engineers - Geotechnical Engineering*. 167 (6), 547–564. Available from: 10.1680/geng.13.00153.

Wan, M. S. P., Standing, J. R., Potts, D. M. & Burland, J. B. (2017) Measured short-term ground surface response to EPBM tunnelling in London Clay. *Géotechnique*. 67 (5), 420–445. Available from: 10.1680/jgeot.16.P.099.

Zhang, G., Guo, Y., Zhou, Y., Ye, M., Chen, R., Zhang, H., Yang, J., Chen, J., Zhang, M., Lian, Y. & Liu, C. (2016) Experimental study on the thermal performance of tunnel lining GHE under groundwater flow. *Applied Thermal Engineering*. 105, 784–795.

Zhang, G., Liu, S., Zhao, X., Ye, M., Chen, R., Zhang, H., Yang, J. & Chen, J. (2017) The coupling effect of ventilation and groundwater flow on the thermal performance of tunnel lining GHEs. *Applied Thermal Engineering*. 112, 595–605.

Zhang, G., Xia, C., Yang, Y., Sun, M. & Zou, Y. (2014) Experimental study on the thermal performance of tunnel lining ground heat exchangers. *Energy and Buildings*. 77, 149–157. Available from: 10.1016/j.enbuild.2014.03.043.

Figure 17 Finite element mesh with stratigraphy, indication of the westbound (WB) and eastbound (EB) tunnels and boundary conditions

Figure 18 (a) permeability profile, (b) pore water pressure profiles in the finite element analyses

Figure 19 Temperature in Analysis A after: (a) 1 month, (b) 6 months, (c) 1 year, (d) 3 years

Figure 20 Thermally-induced surface vertical displacement in Analysis A

Figure 21 Thermally-induced WB tunnel lining deformation in Analysis A: (a) horizontal and vertical axis convergence, (b) deformed shape after 1 year (exaggeration factor: 3000)

Figure 22 Thermally-induced axial force in WB tunnel lining in Analysis A

Figure 23 Total axial force in WB tunnel lining in Analysis A

Figure 24 Thermally-induced pore water pressure in Analysis A after: (a) 1 month, (b) 6 months, (c) 1 year, (d) 3 years

Figure 25 Thermally-induced tunnel lining deformations in Analysis A: (a) horizontal and vertical axis convergence of WB and EB tunnels, (b) deformed shape of WB tunnel after 1 year (exaggeration factor: 3000), (c) deformed shape of EB tunnel after 1 year (exaggeration factor: 3000)

Figure 26 Thermally-induced axial force in EB tunnel lining in Analysis A

Figure 27 Thermally-induced pore water pressure 0.6 m below WB tunnel in analyses A, B1, B2 and B3

Figure 28 Maximum thermally-induced ground vertical displacement above WB tunnel in analyses A, B1, B2 and B3

Figure 29 Maximum thermally-induced axial force in WB tunnel lining in analyses A, B1, B2 and B3

Figure 30 Thermally-induced pore water pressure 0.6 m below WB tunnel in analyses A and C

Figure 31 Maximum thermally-induced ground vertical displacement above WB tunnel in analyses A and C

Figure 32 Thermally-induced WB tunnel lining deformation: (a) horizontal and vertical axis convergence in analyses A and C, (b) deformed shape after 1 year in Analysis A (exaggeration factor: 3000), (c) deformed shape after 1 year in Analysis C (exaggeration factor: 3000)